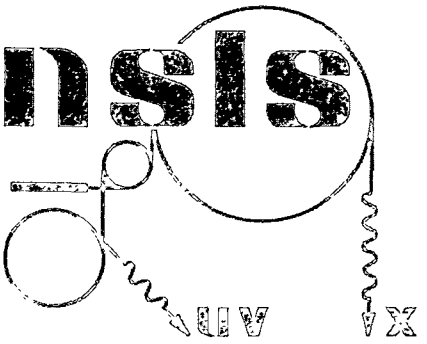

BNL
INFORMAL REPORT
LIMITED DISTRIBUTION

BNL-62447
INFORMAL

HIGH-INTENSITY LASER SYNCHROTRON X-RAY SOURCE

RECEIVED
DEC 27 1995
OSTI

I.V. Pogorelsky

October 1995

NATIONAL SYNCHROTRON LIGHT SOURCE

MASTER

BROOKHAVEN NATIONAL LABORATORY
ASSOCIATED UNIVERSITIES, INC.
UNDER CONTRACT NO. DE-AC02-76CH00016 WITH THE
UNITED STATES DEPARTMENT OF ENERGY
DISTRIBUTION OF THIS DOCUMENT IS UNLIMITED

NOTICE

This report was prepared as an account of work sponsored by the United States Government. Neither the United States nor the United States Department of Energy (DOE), nor any of their employees, nor any of their contractors, subcontractors, or their employees, makes any warranty, express or implied, or assumes any legal liability or responsibility for the accuracy, completeness or usefulness of any information, apparatus, product or process disclosed, or represents that its use would not infringe privately owned rights.

BNL-62447
INFORMAL

HIGH-INTENSITY LASER SYNCHROTRON X-RAY SOURCE

I.V. Pogorelsky

October 1995

DISCLAIMER

This report was prepared as an account of work sponsored by an agency of the United States Government. Neither the United States Government nor any agency thereof, nor any of their employees, makes any warranty, express or implied, or assumes any legal liability or responsibility for the accuracy, completeness, or usefulness of any information, apparatus, product, or process disclosed, or represents that its use would not infringe privately owned rights. Reference herein to any specific commercial product, process, or service by trade name, trademark, manufacturer, or otherwise does not necessarily constitute or imply its endorsement, recommendation, or favoring by the United States Government or any agency thereof. The views and opinions of authors expressed herein do not necessarily state or reflect those of the United States Government or any agency thereof.

HIGH-INTENSITY LASER SYNCHROTRON X-RAY SOURCE

I.V. Pogorelsky
Accelerator Test Facility
National Synchrotron Light Source
Brookhaven National Laboratory
725C, P.O.B. 5000, Upton, NY 11973
Tel: (516) 282-5801, 344-5801
Fax: (516) 282-3115, 344-3115

Summary

A laser interacting with a relativistic electron beam behaves like a virtual wiggler of an extremely short period equal to half of the laser wavelength. This approach opens a route to relatively compact, high-brightness x-ray sources alternative or complementary to conventional synchrotron light sources. Although not new, the Laser Synchrotron Light Source (LSLS) concept is still waiting for a convincing demonstration. Available at the BNL's Accelerator Test Facility (ATF), a high-brightness electron beam and the high-power CO_2 laser may be used as prototype LSLS brick stones. In a feasible demonstration experiment, 10-GW, 100-ps CO_2 laser beam will be brought to a head-on collision with a 10-ps, 0.5-nC, 70 MeV electron bunch. Flashes of well-collimated, up to 9.36-keV (~1Å) x-rays of 10-ps pulse duration, with a flux of ~10^{19} photons/sec will be produced via *linear* Compton backscattering. The x-ray spectrum is tunable proportionally to a variable e-beam energy. A natural short-term extension of the proposed experiment would be further enhancement of the x-ray flux to a 10^{21}-10^{22} photons/sec level, after the ongoing ATF CO_2 laser upgrade to 1 TW peak power and electron bunch shortening to 3 ps. The ATF LSLS x-ray beamline, exceeding by orders of magnitude the peak fluxes attained at the National Synchrotron Light Source (NSLS) x-ray storage ring, may become attractive for certain users, e.g., for biological x-ray microscopy. In addition, a terawatt CO_2 laser will enable harmonic multiplication of the x-ray spectrum via *nonlinear* Compton scattering.

1 Introduction

Generation and application of high-brightness, quasi-monochromatic x-rays and γ-rays is the fast developing area of science and technology. Over the last decade, the NSLS has played a world-wide leading role in providing high-power synchrotron x-ray radiation for advanced multi-disciplinary research. The parameters of the NSLS x-ray source are given in Table 1 [1,2].

These days, numerous applications drive the construction of so-called third generation Synchrotron Light Sources (SLS), designed to deliver x-ray beams in excess of the present NSLS capabilities. These projects are based on an upscale of the traditional SLS technology via the electron beam energy increase and by using more sophisticated undulators (higher-field, longer length, shorter period).

Another major avenue toward bright x-ray beams, which has experienced heavy traffic over the last two decades, is x-ray laser research. The primary challenge on this way is to surpass $(h\nu)^5$-proportional difficulties in creating laser conditions within inner atomic electron shells, which are caused by the fast relaxation of excited levels. Extremely high pumping intensity attainable with state-of-the-art picosecond lasers tightly focused onto solid targets, is the most promising approach to solving this problem [3].

A potential alternative to plasma x-ray lasers is the free electron laser (FEL). Such devices are in operation at visible and IR wavelengths. A proposal has been put forward to build an FEL for the soft x-ray range making use of the 2-mile long linac at SLAC [4].

High-order harmonics generation via nonlinear Thompson or Compton scattering of relativistically strong laser beams in dense plasmas is still another approach to intense x-ray generation. Here, "relativistically strong" means that plasma electron quiver motion driven by such intense laser beams, becomes relativistic. Note, that the names "Thompson or Compton" stand basically for the same effect but described from classical and quantum mechanics positions, correspondingly. Unlike the laser beams, harmonics in plasma are not strongly coherent, monochromatic, or collimated. However this method is attractive due to its relative simplicity and the possibility to produce intense x-ray fluxes. As an example, we refer to the simulated parameters for a hypothetical plasma LSLS driven by a 230 TW laser focused into a 30 μm spot in gas with a stripped electron density $n_e=10^{20}$ cm^{-3}. The λ=4 nm photon flux brightness is expected to be 3×10^{19} photons/s.mm^{2}mrad^2 within a 0.1% bandwidth [5]. Signals demonstrated so far with available realistic lasers are many orders of magnitude weaker.

The x-ray spectral range may be attained much easier when scattered laser photons undergo a Doppler shift on a counter-propagating relativistic electron beam. When we say "easy" we do not mention that a several-MeV electron gun or linac is required according to this method. However, when a relativistic e-beam is available, it pays off by producing scattered photons at the fundamental wavelength of $4\gamma^2$-times shorter than the laser wavelength, where γ is the Lorenzian factor for the e-beam. By the nature of the process, the back-scattered photons are contained within a narrow cone with the apex angle of $\theta=1/\gamma$, and their bandwidth is defined by the momentum spread of the e-beam that may be as low as 0.1%.

With the driving wavelength 10^4-10^5 times shorter than the undulator period, LSLS permits generation of proportionally heavier photons at the same e-beam energy as a conventional SLS, thus providing access to the γ-range. Similarly, LSLS permits the use of ~100 times less energetic electrons to generate x-rays of a particular wavelength, opening the route to relatively compact and inexpensive high-brightness x-ray sources.

Limited by the repetition rate of the laser driver, LSLS can not compete with conventional synchrotron sources in average radiation power. However, it has the potential of delivering extremely intense x-ray flashes in picosecond pulse intervals. Such a regime is of a particular interest for a number of application. As example, we mention one of them - biological x-ray imaging [6].

X-ray microscopes help us to visualize the inside the individual cells, chromosomes and other live objects of submicron size. However, fully developed x-ray imaging requires delivery of an x-ray dose (more than 10^7 rad or 10^{16} photons/cm^2 in the water transmission window between 2.3-4.3 nm) which usually results in the fatal morphological destruction of the object. After receiving such dose, the biological micro-object diffuses or even hydrodynamically explodes, loosing its live features. The characteristic time of such a transformation is less than 1 ns. For capturing holographic images of biological objects at a 30 nm resolution scale, as short as picosecond x-ray pulses would be required.

X-ray beams with 10^{10}-10^{11} photons/pulse may be produced via relativistic Compton backscattering using state-of-the-art terawatt picosecond lasers and high-brightness rf linacs that operate with picosecond photocathode injectors. A quasi-monochromaticity of such x-ray beams permits their tight focusing, with zone plates, into a spot of a ~10 μm size that corresponds to a photon fluence of the order of 10^{16} photons/cm^2. Thus, this approach looks promising to satisfy stringent requirements of x-ray biological imaging and other applications that call for a strong and fast x-ray exposure. Why it was not utilized so far? Maybe because the appropriate laser and linac have never shook hands within one facility. We believe that at the ATF we have such a unique opportunity.

Indeed, the ATF's one of the world-brightest linacs delivers up to 0.5 nC ~10-ps bunches of 70-MeV electrons with a 0.2% momentum spread and normalized emittance of 2 mm.mrad. That permits the high concentration of the relativistic electrons necessary for efficient photon scattering.

Actually, the experimental study of *nonlinear* Compton scattering had been first proposed for the ATF several years ago [7]. That proposal was dedicated to the study of high harmonics generation at a moderate laser power that is more of a basic scientific interest. The optimization of the process towards generating a high-brightness signal at the fundamental frequency has not been specially addressed.

In the present analysis, we shift our emphasis to this subject. Under the present scenario, the primary goals of the proposed experiment would be:

- first, experimentally verify capabilities of the LSLS scheme based upon the combination of a high-brightness electron beam and a high-power CO_2 laser, both of picosecond pulse duration;
- second, to produce high-brightness x-rays useful for NSLS applications;
- and third, to study nonlinear Compton scattering effect.

At the first stage of the experiment, with the presently operational CO_2 laser delivering 10-GW pulses of a 100-ps duration, 9.36-keV (1.3 Å) x-rays of a 10-ps pulse duration with peak fluxes of 1.7×10^{19} photons/s will be obtained.

At the second stage, after the ongoing laser upgrade to the ~1 TW power level (~1997) and the electron bunch shortening to 3 ps , x-ray flashes with peak flux of up to 5×10^{21} photons/sec may be produced. Also, increase of the linac energy to 140 MeV will permit generation of 0.3 Å x-

rays. When the laser and e-beam interact inside a narrow channel, an x-ray brightness (@ 0.1%b.w.) of up to 2.5×10^{22} photons/s.mm^{2}mrad^2 looks possible, that more than an order of magnitude exceeds the peak spectral brightness of the synchrotron radiation in the NSLS x-ray beamline.

The upgraded laser will be strong enough to produce high x-ray harmonics via nonlinear Compton scattering that may be a subject of the third stage of the experiment.

The rest of this paper is organized as follows:

In Section 2, we revise the essentials of linear Compton scattering from the relativistic e-beam.

In Section 3, we give estimates for the x-ray parameters attainable at the ATF at the present time and later, after the CO_2 laser upgrade, and propose the ATF LSLS design.

In Conclusion, we discuss a comparative performance of CO_2 versus solid state terawatt-class laser drivers for prospective high-power LSLS. Prospects for high harmonics generation via nonlinear Compton scattering are briefly addressed.

2 Linear Compton Scattering from a Relativistic Electron Beam

To understand Compton scattering of laser photons at a counter-propagating relativistic electron beam, let us turn to sketches in Fig.1.

The observer resting at the laboratory frame will see a linearly polarized monochromatic electro-magnetic (EM) wave with a frequency ν_L and a phase speed c and electrons propagating in the opposite direction with a speed βc. Assume that the electron meets the EM wave at the point A at phase $\phi=0$, as shown in Fig.1a. After the time interval of $t=1/2\nu_L$, the electron will be at the point B, that is $\sim\lambda_L/2$ away from the point A (we consider $\beta\approx1$). At the same moment, the EM wave arrives to the point B at phase $\phi=2\pi$. Hence, during the time interval $t=1/2\nu_L$ the electron passes the whole period of the wave. From the electron's perspective, the acting EM wave has a double frequency, $2\nu_L$, (see Fig.1b), and the electron has nothing to do but to oscillate with the same frequency (so-called, synchrotron oscillation). Oscillating, the electron generates synchrotron radiation. The electron "thinks" that it radiates secondary EM waves at the same frequency of $2\nu_L$ in both $+z$ and $-z$ directions (still Fig.1b). However, the laboratory observer has a different opinion. Would the electron move exactly at the speed of light, generated photons have no chance to emerge ahead of the electron. This means that the observer would not see scattered photons in the direction of the electron propagation. In reality, the electron is slightly slower than the light propagating in vacuum. Thus, one period of the wave generated by the electron traveling from the point A to the point B shall occupy the interval equal to $\Delta z=c(1-\beta)/2\nu_L$ (as shown in Fig.1c). That will be the wavelength of the backscattered radiation, λ_x, or

$$\lambda_x=(1-\beta)\lambda_L/2. \tag{1a}$$

Using the relation

$$\beta=\sqrt{1-1/\gamma^2}\approx1-1/2\gamma^2 \tag{1b}$$

we obtain

$$\lambda_x=\lambda_L/4\gamma^2. \tag{1}$$

Hence, starting with a laser beam of $\lambda_L=1$ μm (Nd:YAG), or even $\lambda_L=10$ μm (CO_2 laser), and a ~50 MeV electron beam ($\gamma=100$), we obtain backscattered photons in the x-ray region (0.25Å or 2.5Å, correspondingly). Similarly, one period of the wave radiated by the electron in the opposite direction occupies the interval $\Delta z=\lambda_L$. Having destructive interference with the passing incident EM wave, this component is responsible for the observed depletion of the transmitted laser beam.

An equally simple consideration helps to understand the narrow anguiar divergence of the backscattered radiation. Indeed, the laboratory observer stops to see backscattered photons when the projection of their speed onto the z-axis is equal or smaller than βc. Addressing Fig.2, we see that no photons should appear beyond the cone with the apex angle $\theta\geq cos^{-1}\beta$. Using (1b) and expansion

$$\cos\theta\approx1-\frac{1}{2}\theta^2,$$

we come to the angular divergence of the backscattered photons equal to

$$\theta_o = 1/\gamma. \quad (2)$$

Hence, the backscattered photons are generated within a narrow cone with a solid angle $\Omega = 2\pi\theta_o^2$. Within this cone, the scattered radiation frequency drops off axis according to

$$\frac{\Delta\omega}{\omega_x} \approx \gamma^2 \Delta\theta^2, \text{ hence, } \frac{\Delta\omega}{\omega_x} \approx 1 \text{ over } \Delta\theta = \theta_o.$$

For every particular observation angle, the radiation spectrum is sharply peaked around its local frequency. Note that only the infinitely long wave may be ideally monochromatic. The fractional bandwidth of the electron's radiation will depend upon the total number of laser wavelengths N over the electron-laser interaction distance:

$$\Delta\lambda'_x/\lambda_x = 1/N. \quad (3)$$

It also follows from (1) that the bandwidth of the backscattered x-rays is directly related to the momentum spread or the "temperature" of the e-beam as

$$\Delta\lambda''_x/\lambda_x = 2\Delta\gamma/\gamma. \quad (4)$$

In general, there is also an additional longitudinal e-beam energy spread due to emittance. However, this component is negligible for the low-emittance ATF e-beam and for considered below e-beam focusing conditions. Then, the total bandwidth is equal to:

$$\Delta\lambda_x = \sqrt{\Delta\lambda''^2_x + \Delta\lambda'^2_x}. \quad (5)$$

This narrow bandwidth radiation is observed within the cone with the opening angle

$$\theta_f \approx (\Delta\lambda_x/\lambda_x)^{1/2}/\gamma.$$

Discussed above angular and spectral distributions of the backscattered radiation enter into the expression for spectral brightness, B, which is a cumulative characteristic of the radiation source that depends also upon the radiated power, P_x, and radius of the laser/e-beam interaction area, R,

$$B = \frac{P_x}{(2\pi R\theta)^2 \Delta\nu_x}. \quad (6)$$

According to classical electrodynamics, an accelerated electron emits radiation with a power

$$P_e = 2e^2\dot{\bar{V}}^2/3c^2, \quad (7)$$

where $\dot{\bar{V}}$ is the acceleration vector (averaged over the oscillation period) defined by the acting oscillatory electric field of the EM wave

$$\dot{\bar{V}} = eE_L/m \quad (8)$$

and $|E_L|$ is related to the laser intensity $I_L = P_L/\pi r_L^2$ via

$$|E_L|^2 = 2I_L/\varepsilon_0 c \text{ or } |E_L|[\text{TV/m}] = 2.6\times10^{-9} I_L^{1/2}[\text{W/cm}^2]. \quad (9)$$

Here P_L and r_L are the laser beam power and radius. Combining (7)-(9), we obtain

$$P_e \sim P_L r_e^2/r_L^2, \quad (10)$$

where $r_e=e^2/mc^2=2.82\times10^{-13}$ cm is the classical electron radius.

Expression for P_e corrected for the relativistic electron motion in a Gaussian laser beam has been obtained in [5]

$$P_e=\frac{64}{3}P_L r_e^2\gamma^2/r_L^2. \tag{11}$$

Considering for simplicity the rectangular laser pulse of the duration τ_L and a uniform electron distribution with a density n_e over the e-bunch length τ_b, the power radiated by the electron ensemble within the immediate interaction region $L(t)$ is equal to

$$P_x(t)=P_e n_e L(t) S_L, \tag{12}$$

where $L(t)$ at any moment t is equal to or smaller than $min\{c\tau_L, c\tau_b\}$, and $S_L=\pi r_L^2/2$ is the effective cross-section for Gaussian laser beam [5]. The radiation process will continue during the time interval while the laser pulse and the electron bunch are at least in a partial intersection. It is presumed that the e-beam radius r_b matches or is bigger than r_L and, hence, the total laser power is used efficiently. Then, the total backward scattered radiation energy is

$$E_x=\int_0^{(\tau_L+\tau_b)/2} P_x(t)dt = P_e n_e S_L c\left[\min\{\tau_L,\tau_b\}\left(\frac{1}{2}\min\{\tau_L,\tau_b\}+\left|\frac{\tau_L-\tau_b}{2}\right|\right)\right]= P_e n_e S_L c\frac{\tau_L\tau_b}{2}. \tag{13}$$

Note that the actual duration of the produced backscattered pulse is not necessarily equal to the total laser-electron interaction time interval

$$\tau_{int}=(\tau_L+\tau_b)/2.$$

Since x-rays originate from electrons in the direction of the electron propagation, it turns out that the x-ray pulse length is defined primarily by the electron bunch duration (see Fig.3). On top of it is the x-ray pulse stretching due to the x-ray and electron speed mismatch accumulated over the interaction time

$$\Delta\tau=(1-\beta)\frac{\tau_L+\tau_b}{2}\approx\frac{\tau_L+\tau_b}{4\gamma^2}. \tag{14}$$

Hence, the total x-ray pulse duration is

$$\tau_x=\tau_b+\Delta\tau=\frac{1-\beta}{2}\tau_L+\frac{3-\beta}{2}\tau_b\approx\tau_b+\frac{\tau_L}{4\gamma^2}. \tag{15}$$

However, for the practically important case when $\tau_L<<4\gamma^2\tau_b$ (see Section 3), $\tau_x\approx\tau_b$. It follows that relatively long laser pulses may be tolerated without a noticeable increase in the x-ray pulse duration. Combining (11) and (13), the x-ray power is

$$P_x=\frac{E_x}{\tau_x}\approx\frac{32\pi}{3}E_L n_e c\gamma^2 r_e^2\approx\frac{10E_L Q\gamma^2 r_e^2}{e\tau_b r_b^2}, \tag{16}$$

where $E_L=P_L\tau_L$ is the laser pulse energy, Q is the electron bunch charge and r_b is the e-beam radius in the interaction region (we consider $r_b\geq r_L$, so that no laser energy is lost for interaction). Corresponding to (16) the engineering formula is

$$P_x[W]\approx\frac{0.5E_L[J]Q[nC]\gamma^2}{\tau_b[ps]r_b^2[mm]} \tag{16a}$$

The conclusion drawn from (16) is the insensitivity of the produced x-ray power upon the laser pulse duration. The high total laser pulse energy, short-duration of the relativistic electron bunch, and high spatial concentration of electrons within the bunch become the most important parameters that define the x-ray peak power.

Similarly, as follows from (16), there is no immediate requirement for the tight focusing of the laser beam in order to produce intense x-rays.

All these features are quite understandable as long as we talk about the *linear* Compton process, the efficiency of which, by definition, should not depend upon the laser intensity (power per unit area). However, the plain conclusion that the x-ray intensity does not depend at all upon the laser pulse duration and upon the laser beam focusing would not be correct. The thing is that the proportionality of P_x to $1/r_b^2$ requires the tight focusing of the e-beam in the interaction region. In order to be in a good overlap with the electron beam, the laser beam shall be focused to the same or smaller spot size.

Because of the natural divergence of the electron and laser beams, they remain tightly focused only within a limited distance L_{int}. For the Gaussian optical beam, this distance is related to the Rayleigh length, z_0, measured from the focal point to the point where the laser beam expands two times in a cross-sectional area, by the ratio

$$L_{int}^{L} \approx \pi z_0 = \pi^2 r_L^2 / \lambda_L. \tag{17}$$

A similar condition is applicable to electron beams with their divergence characterized by geometric emittance ε/γ in the same way as diffraction-limited laser beams are characterized by wavelength,

$$L_{int}^{b} = \pi^2 r_b^2 \gamma / \varepsilon. \tag{18}$$

The comparison of λ_L with ε/γ tells which one - e-beam or laser beam - is the limiting factor for making the interaction region narrow. For instance, the ATF low-emittance (2 mm.mrad @ 50 MeV) electron beam permits, in principle, much better filamentation than the geometrically focused CO_2 laser beam. Thus we consider below that limitations to L_{int} are imposed by the laser beam.

For the efficient use of the laser pulse in the Compton process, the laser beam waist, L_{int}^{L}, shall extend over the overlap distance defined by the electron and laser pulse duration

$$2L_{int}^{L} \geq c(\tau_L + \tau_b). \tag{19}$$

If L_{int} is below the limit defined by (19), it may result in the proportional drop of the laser energy coupled to the electron bunch. Thus, overly-tight laser focusing would not help to gain any additional x-ray power. From (17) and (19), it follows that, at $\tau_L \geq \tau_b$, laser parameters shall also satisfy the condition

$$r_L^2 \geq \frac{c\tau_L \lambda_L}{2\pi^2}. \tag{20}$$

Combining (20) with (16a) and assuming $r_b = r_L$, we obtain the estimate for the maximum attainable x-ray power, when only the laser beam divergence puts the limit to the length and cross-section of the interaction area,

$$\frac{P_x^{max}}{P_L} \approx 3 \times 10^{-8} Q_{[nC]} \gamma^2 / \tau_{b[ps]} \lambda_{L[\mu m]}. \qquad (21)$$

Certainly, (16) is still valid and especially meaningful when the dimensions of the interaction region are chosen above the numbers set by the optical restrictions, e.g., when realistic r_b is still above the limit set by (20).

It is beyond the scope of the present study to propose any particular application for the LSLS. Each application may have special requirements to x-ray wavelength and intensity. To reach any particular wavelength through linear Compton backscattering, one should make his choice of λ_L and γ as according to (1). However, it would be instructive to mention that, in order to produce x-rays of high intensity and brightness, it is beneficial to choose possibly high values for both parameters, λ_L and γ. To illustrate this idea, let us compare CO_2 (λ_L=10 μm) and Nd:YAG (λ_L=1 μm) lasers of equal power. Containing 10 times more photons, CO_2 laser beam will be responsible for 10 times more scattering events. As long as the electron's γ-factor is chosen proportionally to $\sqrt{\lambda_L}$, the emerging x-ray photons are of equal energy for both cases. Hence, the generated x-ray power is 10 times higher for CO_2 laser driver.

The above remark on the advantage of a long-wavelength CO_2 laser is valid provided other parameters entering to (16) are equal. In a situation when the cross-section of the interaction region is limited by the diffraction divergence of the laser beam, which is proportional to λ_L, P_x does not depend any more upon λ_L. This conclusion follows from (21) under the assumed above condition of $\gamma \sim \sqrt{\lambda_L}$. However, it is likely that the radius of the interaction region will not be reduced much below 30 μm due to such practical considerations as alignment and pointing stability of the laser and e-beam. We show below that focusing to r_L=30 μm may be obtained with the CO_2 laser. Under this assumption, the wavelength power scaling discussed above is still valid.

Note also that the dependence of the angular divergence (2), spectral bandwidth (4), and brightness (6) upon γ adds to the consideration of choosing possibly high γ values for a high-brightness x-ray LSLS.

The x-ray flux and brightness levels attainable with the ATF electron beam and laser parameters will be discussed in the next Section.

3 Feasibility of High-Intensity X-Ray Experiments at the ATF

3.1. ATF Operational Status

We start with a description of the Accelerator Test Facility at BNL relevant to understanding the technical feasibility of the x-ray LSLS experiment.

ATF OVERVIEW

The ATF is a user's facility dedicated to the research of physical phenomena at the interaction of high-brightness electron beams with laser radiation. For this mission, the ATF is equipped with a laser photocathode rf-gun, an electron linac, high power short pulse lasers synchronized with the electron beam, and appropriate diagnostic equipment.

Fig.4 presents the diagram of the ATF. The laser system consists of Nd:YAG and CO_2 lasers. The 1.06 μm, 10-ps, 1 GW Nd:YAG laser serves for picosecond slicing in the CO_2 laser system and, after frequency quadrupling, as a linac photocathode driver. The 10.6 μm, 100-ps, 10 GW CO_2 laser beam is transported to several locations in the experimental hall, where it interacts with e-bunches to test different laser accelerator schemes.

The 10-ps bunches of 5-MeV electrons with up to 1 nC charge, are produced at a laser photocathode electron gun with a 3 Hz repetition rate and are accelerated to 50-70 MeV by two RF traveling-wave linac sections.

Electron beam is supplied to several experiments parked in three parallel beamlines. Three experiments - Inverse Cherenkov Laser Accelerator, (ICLA) Inverse FEL Accelerator, and Visible FEL - are presently active. Two other - High-Gain Harmonic Generation and Grating Linac - are in preparation. The proposed location of the LSLS experiment is downstream of the ICLA experiment.

LINAC

Electrons originate from a photocathode in the rf-gun. Copper photocathode with a quantum efficiency of ~10^{-4} requires 50 μJ energy of the Nd:YAG 4th harmonic (λ=0.26 μm) to produce photoelectrons of a 1 nC total charge. In the rf-gun, with a $1\frac{1}{2}$ cell cavity resonant to a 2856 MHz rf-field driven from a klystron to as high as 12.5 MW power, photoelectrons are accelerated to 5 MeV by a 100 MV/m cathode field. Produced electrons are of ~2 mm-mrad normalized emittance and a 17 keV energy spread due to the short laser pulse duration. The electron bunch duration defined by the Nd:YAG 4th harmonic is ~10 ps. Plans have been put forward to reduce the e-bunch to ~3 ps by a nonlinear compression of the UV photocathode driver pulse and its wave-front tilt correction.

The ATF linac consists of two 3 m long, traveling wave linac sections driven by a 25 MW 2856 MHz klystron with a pulse duration of 3.5 μs at up to 6 Hz (regularly 3 Hz) repetition rate. Presently operated at 50-70 MeV energy, linac permits upgrade to 100-140 MeV if a klystron for each accelerating section is provided.

Two collimators with variable aperture incorporated in the post-linac beam transport line define small emittance e-beam for the laser acceleration experiments.

The presently available electron beam diagnostics incorporate strip-line monitors for non-destructive measurements of energy, current and beam position, remotely controlled beam profile monitors based on phosphor screens and CCD cameras, and Faraday caps for beam charge measurements. Higher resolution beam profile monitors based on observation of transient radiation from metal mirrors are under test.

Three high-energy beamlines, accommodated in the experimental hall, permit supply of the electron beam to several experiments that may be serviced nearly in parallel.

The operational characteristics of linac are summarized in Table 2 that presents also the essential parameters of the ATF laser system.

BEAMLINE #1

After the linac and collimator, the electron beam transport line enters the experimental hall. The ATF beamline #1, branched by a dipole from the main beamline, is the most likely location for the x-ray experiment. The present layout of beamline #1 is shown in Fig.5. The magnets setup is designed to serve three experiments located along the beamline [8]. These experiments are: Laser Linac (Grating Accelerator), Inverse Cherenkov Laser Accelerator, and Compton Scattering. The positions of these experiments are shown in the drawing. Each experiment has different requirements to the e-beam that shall be delivered to the interaction region. The most critical is the sub-micron e-beam size required for the Grating Accelerator. This requirement drives the design of the final focus system consisting of 6 quadruples serving to focus the e-beam to r_b=0.8 μm over the Rayleigh length of 1.3 mm, and two recollimating quadrupoles that send the beam towards the electron spectrometer at the end of the beamline. The requirements towards the e-beam focusing for other two in-line experiments (ICLA and Compton scattering) are much less stringent (~100 μm wide e-beam would be desirable for both experiments.) These requirements may be satisfied by the proper electric current settings of the same magnet system. Two additional steering coils are introduced to control the alignment of the e-beam along the focused CO_2 laser beam. The interaction gas cell of the ICLA experiment is placed on kinematic mounts and is easily removable. That permits transport of the e-beam to the downstream location previously intended for the nonlinear Compton experiment and presently unoccupied. For a possibility to produce a tightly focused beam in this location we refer to TRANSPORT simulations [9]. At the assumed rather pessimistic emittance of 5 mm.mrad and momentum spread of 0.5%, the simulated e-beam radius in the location of the ICLA experiment is $r_b(\sigma)\approx$100 μm. We may assume similar or even better focusing in the position of the Compton experiment with recently demonstrated ATF e-beam parameters of ε=2 mm.mrad and $\delta p/p$=0.2%. If tighter e-beam focusing is required, additional quadrupoles may be placed before the interaction point, bringing the e-beam waist down to several microns [8]. Another option is to move the x-ray LSLS experiment to the position of the projected Grating Accelerator experiment.

LASERS

The diagram in Fig.6 shows main subcomponents of the ATF laser system and illustrates joint operation of YAG and CO_2 lasers serving for the projected x-ray experiment. Actively mode-locked CW YAG oscillator generates a train of 12-ns spaced 15-ps pulses of linearly polarized

radiation at λ=1.06 μm, synchronized to a subharmonic of the linac RF field. A Pockels cell switch, in combination with a polarizer, cuts out single pulses in a 3 Hz sequence. After 4-pass preamplifier and double-pass amplifier, pulses acquire 20 mJ energy. Part of this energy is split to control picosecond slicing in the CO_2 laser system. Other portion is directed through the 2nd and then 4th harmonic crystals to a photocathode generating 12-ps electron bunches.

Application of a mode-locked laser as a RF gun driver puts strict requirements on the stability of all laser parameters. Bigger instabilities than those specified in Table 2 would result in unacceptably high variations of accelerated electrons energy, beam emittance, aberrations, etc. Such stringent requirements to the stability are satisfied by using a diode-pumped laser oscillator that is characterized by appropriately small jitters in power and mode-lock timing. Also, we use relay imaging and spatial filtering throughout the system, with long portions of beam path enclosed in evacuated tubes.

CO_2 laser delivers high-power pulses of IR radiation synchronized with the electron bunches. Such synchronization is automatically achieved by semiconductor optical switching of a several picosecond pulse out of a 100-ns 1-MW oscillator output using the same Nd:YAG laser pulse which is ultimately used to drive a photocathode. YAG pulse, having photon energy above the band gap of a semiconductor (Ge), creates an electron-hole plasma in a surface layer. When the plasma reaches critical density refractive index becomes imaginary, and Ge, that is normally transparent to 10-μm radiation, turns into a high reflector. After the control pulse termination, the drop of the reflection from the Ge has a characteristic time of diffusion of the free-carriers into the bulk material, 150 ps. To define the trailing edge of the pulse, shortening it to a few picoseconds, transmission switching, the complement to reflection switching, is used for the second stage. Using the same fast laser initiator for the linac and CO_2 laser ensures the desired picosecond synchronization of the electron bunch and laser pulse at their interaction point.

The sliced pulse is transmitted through the 3-atm, UV-preionized, 120-cm long amplifier energized by a 150-kV pulsed discharge. The first four passes are arranged in a double-X configuration using a 4-mirror set-up. To increase the total gain to ~10^5, the beam is redirected for the next 4 passes through the amplifier. The active Pockels optical isolator, in combination with a passive plasma shutter, prevents parasitic self-lasing, otherwise inevitable in such a scheme.

Ultimately, after 8 passes through the amplifier we measure 1 J output energy in a 100-ps pulse, which corresponds to the spectral-bandwidth-limited minimum pulse duration sustained by the 3-atm CO_2 amplifier. Amplified to 10 GW peak power, CO_2 laser pulses are transported to the experimental hall where they are used for various experiments.

Most of the ATF experiments, under way or planned, will greatly benefit from the further CO_2 laser power increase over the existing 10-GW peak power. Based upon the capabilities of present laser technology and the modeling results of picosecond pulse amplification already verified experimentally at the ATF, it has been shown that a relatively compact single-beam picosecond CO_2 system, with one big-aperture amplifier stage, is potentially scalable to the terawatt peak power level.[10].

The upgraded ATF CO_2 laser system will incorporate an x-ray preionized, multi-atmosphere, multi-isotope, big aperture CO_2 laser amplifier. The project is planned for completion in 1997. The upgraded laser system will be capable to produce 3-5 ps pulses at or above 1 TW peak power (up to 4 TW with a multi-isotope CO_2 gas mixture) with a repetition rate of 0.1 pps. However, such shortening of the CO_2 laser pulse may result in the increase of the x-ray spectral bandwidth as according to (3). For linear Compton scattering, a longer (about 50 ps) laser pulse

may be an optimal choice. The output laser energy will be limited to ~15 J by the optical damage threshold of the amplifier output window.

3.2. Design Parameters for the X-Ray LSLS Experiment

In this paragraph, we consider the expected performance of the LSLS based on linear relativistic Compton backscattering of picosecond CO_2 laser pulses on counter-propagating picosecond electron bunches. This configuration may be realized at the ATF with its presently available 10 GW, 100-ps CO_2 laser and 10(or 3)-ps, 0.5 nC, 70 MeV electron beam. For the electron beam, we assume an emittance of ε=2 mm.mrad and momentum spread of $\delta p/p$=0.2%, as already demonstrated at the ATF. For the upgraded LSLS versions, we will consider a 1-TW 5-ps or 0.3-TW, 50-ps CO_2 laser pulse and a 3-ps, 70-MeV or 140-MeV e-beam.

By (1), the wavelength of the backscattered radiation will be

$$\lambda_X=\lambda_L/4\gamma^2=1.325 \text{ Å} \text{ @ } E_e=70 \text{ MeV}, \lambda_L=10.6 \text{ μm}.$$

That corresponds to the photon energy of $h\nu_X$[eV]=$1.25\times10^4/\lambda_X$[Å]=9.36 keV=1.5×10^{-15} Joules.

Spectral tuning of the generated x-rays is possible via E_e adjustment. Be aware that the x-ray power (16) will vary proportionally to E_e^2, and the x-ray brightness (6) will vary proportionally to E_e^5. Another way to change the x-ray wavelength is by tuning the CO_2 laser wavelength within the CO_2 gain spectrum (9.2-11.8 μm). Quantitative estimates below are done for λ_X=1.325 Å.

Defined by (5), the intrinsic spectral bandwidth of the backscattered x-rays is

$$\Delta\lambda''_X/\lambda_X\approx2\Delta\gamma/\gamma=4\times10^{-3}.$$

By (2), the angular divergence of the backscattered photons is equal to $\theta=1/\gamma$=7 mrad.

According to (19), the length of the interaction region, where the focused laser beam matches in a cross-section the counter-propagating e-beam, is

$$L_{int}\approx c(\tau_L+\tau_b)/2=17 \text{ mm}, \text{ @ } \tau_b=10 \text{ ps and } \tau_L=100 \text{ ps}.$$

As discussed in Section 2, the comparison of λ_L with ε/γ tells which one - e-beam or laser beam - is the principal limiting factor for making the interaction region narrow. The geometric emittance, demonstrated at the ATF, of $\varepsilon/\gamma=2\times10^{-2}$μm.rad, being orders of magnitude smaller than the CO_2 laser wavelength, λ_L=10.6 μm, indicates that the CO_2 beam's limited focusability will ultimately define the effective radius of the interaction region. Using (17), we calculate the waist radius of the diffraction limited CO_2 laser beam to be

$$r_L=\sqrt{L_{int}\lambda_L}/\pi\approx140 \text{ μm}.$$

Hence, the e-beam shall be focused to the same size, r_b=140 μm. Such focusing shall be possible with the present magnet configuration in the ATF beamline #1 at the proposed position of the Compton Scattering experiment (see Fig.4 and 5). (Note, that much tighter, submicron, e-beam focusing may be produced in the position of the Grating Accelerator experiment.)

According to (15), the duration of the backscattered x-ray pulse will be $\tau_x\approx\tau_b$=10 ps (3 ps with the upgraded photocathode Nd:YAG laser driver).

We assume that the total laser energy is delivered into the interaction region without noticeable transport losses. At the above specified laser and e-beam parameters, the total

backscattered x-ray power and flux, according to (16a), are, correspondingly P_x=25 kW, $F\approx 1.7\times 10^{19}$ photons/sec, @τ_b=10 ps, and P_x=80 kW, $F\approx 5.3\times 10^{19}$ photons/sec, @τ_b=3 ps. The total x-ray pulse energy or the total number of the x-ray photons per pulse will be for both cases equal to $\sim 1.7\times 10^8$ photons/pulse. (Here and below, we estimate x-ray fluxes under the approximation of the uniform photon energy equal to that measured along the e-beam axis.)

Shortening of the electron bunch to 3 ps will result in a considerable reduction of its momentum spread which, in the first approximation, is proportional to $\delta p/p\sim\tau_b^2$. Assuming, under these conditions, the spectral width of x-ray radiation to be $\Delta\lambda_X/\lambda_X\approx 10^{-3}$, the peak x-ray brightness at τ_b=3 ps, calculated by (6) and averaged over the entire solid angle $\Omega = 2\pi\theta_0^2$ is B(/0.1% b.w.) $\approx 10^{18}$ photons/sec.mm^{2}mrad^2. Note that the expressions for angular and spectral distributions of the backscattered radiation are quite complex [5]. More accurate calculations of the spectral brightness or quasi-monochromatic fluxes of the backscattered x-rays would be beyond the scope of this introductory paper.

We consider the demonstration of the estimated above results as a proof-of-principle of the LSLS that will complete Stage 1 of the proposed study. At Stage 2, after the projected upgrade of the ATF CO_2 laser system, 1-TW (5-ps) or 0.3-TW (50-ps) laser pulses will be produced, giving a promise of much higher LSLS performance as estimated below.

With the 50-ps CO_2 laser upgraded to 15 J of output energy (Table 4), the x-ray flux will be increased proportionally to the level of $F\approx 8\times 10^{20}$ photons/sec, @τ_b=3 ps. The total number of x-ray photons per pulse is equal now to $\sim 2.5\times 10^9$ and the peak brightness B(/0.1% b.w.)$\approx 1.5\times 10^{19}$ photons/sec.mm^{2}mrad^2.

Note, that with a short, 5-ps laser pulse, the x-ray intensity increase will be attained, according to (16), due to the shortening of the interaction region that permits tighter focusing of the laser and electron beams. With the short interaction length L_{int}=1.2 mm (defined by the short laser and electron pulses, correspondingly, both 5 ps and 3 ps), the laser beam waist may be brought to r_L=30 μm. Assuming the corresponding focusing of the e-beam, the expected 9.36 keV x-ray peak flux will be increased to $F\approx 5\times 10^{21}$ photons/sec. The total x-ray photon number in this case is $\sim 1.5\times 10^{10}$ photons/pulse. Because of the short laser pulse, the x-ray spectrum will broaden, according to (3), to $\Delta\lambda'_X/\lambda_X\approx 0.6\%$. The angle-averaged brightness is B(0.6% b.w.)$\approx 2\times 10^{21}$ photons/sec.mm^{2}mrad^2 or B(0.1% b.w.)$\approx 3\times 10^{20}$ photons/sec.mm^{2}mrad^2(/0.6% b.w.) (see Table 5)

It becomes evident that, in order to maintain a high monochromaticity, the CO_2 laser pulse duration shall be of the order of 50 ps or longer. The contradiction involved in the desire to have a long interaction distance with a narrow cross-section may be, in-principle, resolved by channeling the laser beam. The idea of laser beam channeling, relevant also for such applications as x-ray lasers, beat-wave and wake-field laser accelerators, and laser fusion, is presently under extensive study. This subject has been reviewed in [11].

If to compare with parameters of the free-space interaction summarized in Table 4, the channeled to $r_L=r_e$=30 μm, 50-ps laser beam and a 3-ps electron beam can produce 20 times higher x-ray flux and 400 times higher brightness within the same narrow, 0.1% spectral bandwidth (see Table 6).

As mentioned above, the ATF linac is readily upgradable to 140 MeV. According to (1), the x-ray wavelength will be reduced to λ_X=0.33 Å or $h\nu$=37 keV. A 140-MeV e-beam will

increase the ATF LSLS brightness to $B(0.1\%\ \text{b.w.}) \approx 2.5\times10^{22}$photons/sec.mm^{2}mrad^2 due to the 2-times smaller x-ray divergence.

Note, that as long as the x-ray photon energy and the total x-ray power are both proportional to γ^2, the number of backscattered photons should not depend upon the electron energy. Thus, tuning the LSLS to the softer x-ray region is possible without photon flux reduction. For example, by tuning the e-beam energy to 16 MeV (γ=32), one gets x-rays of 500 eV energy, within the "water window" interesting for biological applications. The calculated above photon fluxes are very close to numbers desirable for high-resolution x-ray microscopy of live objects (see Section 1).

We should understand that the reduction in γ does not go without pain. The x-ray monochromaticity and angular divergence will be proportionally compromised (see (2) and (4)). However, the detailed analysis of possible applications of the ATF LSLS is beyond the scope of the present study.

3.3. Configuration of the X-Ray LSLS Experiment

Principal scheme for the x-ray LSLS experiment at the ATF is similar to one formerly proposed for the Nonlinear Compton Scattering experiment [7]. Main components of the experiment are:

- interaction vacuum chamber with an optics assembly for focusing and directing the laser beam,
- focusing and steering electromagnets for the e-beam,
- x-ray spectrograph and detectors.

The beamline #1 magnet system to be used in the experiment has been described in [8,9]. The principal design of the x-ray Bragg spectrograph was discussed in [7]. Here, we discuss in more detail the configuration of the IR optical system proposed for the experiment.

The preferred location of the LSLS experiment is at the end of the ATF beamline #1, between the ICLA interaction chamber and the bending dipole magnet of the electron spectrometer. The manifold of quadruples and steering magnets located upstream of the ICLA experiment will serve for focusing and pointing the e-beam to the LSLS interaction region. To make it possible, the kinematic ICLA chamber will be removed from the beamline. If necessary for tight focusing (r_b=30 μm), additional quadrupoles may be positioned before the LSLS interaction cell.

The LSLS interaction vacuum cell accommodates the following primary components:

a) optics that redirect the sidewise incident CO_2 laser beam, focus it onto the e-beam axis, and extract the spent beam for diagnostics;

b) two pop-in phosphor screens that could be remotely inserted at the ends of the interaction region to control the e-beam size and position;

c) downstream pop-in Al-coated mirror to introduce the alignment HeNe laser beam;

d) optional capillary tube and capillary holder permitting its 2-axis translation and 2-axis tilt.

The focal length, F, of the focusing element (lens or mirror) is defined by the required radius of the laser beam in the interaction region, r_L, and by the initial laser beam divergence φ. Assuming the diffraction-limited, collimated, Gaussian incident beam,

$$r_L=F\varphi \text{ with } \varphi=M^2\lambda/\pi R,$$

where R is the laser beam radius at the focusing element, and M^2 is the quality factor that characterizes how much the intrinsic divergence of the collimated beam exceeds the diffraction limit (for the ideal diffraction limited beam, $M^2=1$). Combining the above two expressions, we obtain

$$F=\frac{r_L\pi R}{\lambda_L M^2}. \tag{22}$$

The quality factor M^2 for the realistic laser beam used in the experiment may be verified prior to finalizing the focusing element by fitting the measured propagation characteristics of the beam into the beam tracing program (e.g., BEAMCAD). A long focal length lens, IR camera, and Spiricon beam analyzer are the components necessary for such measurements. By applying this procedure to the laser beam delivered with the present ATF CO_2 laser, we have verified that its natural divergence is $M^2\approx1.5$, very close to the diffraction limit. Eq.(22) shows that controlling the beam diameter on the focusing element helps to maintain the required waist size. That actually relaxes the requirements to the accuracy of measuring M^2 or specifying F.

The minimum acceptable laser beam radius, R, is defined by the damage threshold of the focusing element. For a high-quality Cu mirror illuminated with CO_2 pulses of a picosecond duration, the damage threshold is 5 J/cm^2 [12]. Assuming close to the Gaussian laser beam profile, we consider that, for damage-safe operation, the following condition shall be satisfied: $E_L/\pi R^2\leq2$ J/cm^2. For the present 1-J ATF CO_2 laser pulse, this condition brings us to $R\geq4$ mm. For the CO_2 laser upgraded to the 15-J pulse energy, $R\geq16$ mm.

For every particular case, F shall be chosen according to (22). Hence, it is F=80 mm, @ E_L=1 J and r_L=100 μm, and F=320 mm, @ E_L=15 J and r_L=100 μm. For r_L=30 μm, desirable when a short laser pulse of a 5-ps duration or a channeled laser beam is used, the focal length of the focusing mirror shall be reduced to 24 mm and 100 mm, @ E_L=1 J and E_L=15 J, correspondingly, with the f-number, defined as a ratio of the mirror focal length to its diameter, $f=F/\varnothing$, being for both cases ~3.

Manufacturing of the aberration-free focusing element with such low f-number is, in principle, possible with the state-of-the-art computer-controlled diamond tuning technique. However, this problem may be simplified if we use a converging laser beam incident onto the final focusing mirror. The expansion of the input laser beam above its size calculated at the Cu mirror will be necessary in order to introduce the beam into the interaction cell through the transparent window or lens that separates the vacuum cell from the ambient. The minimum radius, R', for the input beam is limited by the optical damage threshold of the input window material. The damage threshold for ZnSe and NaCl - typical window materials for CO_2 laser radiation - is estimated to be 0.5 J/cm^2 [12] which is 10 times less than for a Cu mirror. Correspondingly, the illuminated area of the window shall be at least 10 times bigger than of the mirror resulting in $R'/R=\sqrt{10}$.

The equivalent lens system in Fig.7 illustrates this scheme that gives also a possibility to increase f-number two times above the low values calculated so far. Distance from the last focusing element to the waist center, S, is defined by

$$S = \frac{F(F'-d)}{F+F'-d} \tag{23}$$

In order to determine the waist radius for this scheme, we just need to substitute F by S in (22). Hence, all the above estimates for the focal length are valid now for S, and F will depend upon the choice of F' and d. This choice is narrowed due to the additional requirement of the equal f-number for both focusing elements, $F/R=F'/R'$. (This assumption just means that we do not want to solve the technological problem associated with a small f-number for one focusing element by transferring it to another element.) Under this condition, we get $F=F'-d$ and, by (23), $S=F/2$.

To be more specific, we calculate parameters of the optical system designed for the case of r_L=30 μm and E_L=15 J: F=200 mm, ∅=40 mm, F'=660 mm, ∅'=120 mm, and d=460 mm. The required big diameter of the first focusing element makes it impractical to use a lens as an input optical window to the vacuum cell. Close to 100 kg mechanical stress at the vacuum/air interface will introduce distortions and aberrations to the lens. Instead, we propose a massive anti-reflection coated window manufactured of ZnSe or NaCl and two focusing Cu mirrors inside the vacuum cell. Two of various possible optic configurations are illustrated in Fig.8. Because of the off-axis incidence and reflection, the reflective surfaces shall have an aspherical, close to parabolic, shape. The final mirror is drilled to the minimum diameter of 2 mm in order to transmit the e-beam and x-rays with the expected divergence of 7 mrad. However, such small aperture may be too restrictive at more flexible experimental conditions. For example, e-beam energy reduction below 70 MeV for softer x-ray production results in proportionally higher angular divergence of the produced x-rays. To permit such options, the hole drilled through the mirror shall be increased in diameter to 10-15 mm. In order not to lose the laser energy and initiate plasma at the edges of the hole, it would be preferable to use a "donut"-shaped laser beam having zero intensity at the center. Such a laser beam profile may be produced with an axicon telescope prior to the laser beam entering into the cell. Fig.9 illustrates this approach.

The proposed principal layout for the LSLS experiment is shown in Fig.10. We show lenses inside the vacuum chamber just in order to simplify the drawing. The preferred optical configuration incorporates metal focusing elements as illustrated in Fig.9.

Diverging after the interaction region, the spent laser beam is reflected off the e-beam axis by a flat Cu mirror and exits the cell through the output window similar to the input one. The flat mirror has a several-millimeters drilled hole to transmit the e-beam to the interaction region. Placed onto the remotely controlled translation stage and movable in the direction parallel to its reflective surface, the flat mirror also permits reflection of the alignment HeNe laser beam when the drilled hole is displaced from the beam axis.

The spent laser beam is directed to the beam-dump and for energy measurement. Selected with a beamsplitter and further attenuated, a small portion of the beam energy is directed to the optical imaging system. This system, that consists of two ZnSe lenses of the total ~10 times magnification, pyroelectric IR viewer and CCD camera, serves for high-resolution measurements of the laser and e-beam spot sizes as well as to control their positioning (alignment) inside the interaction region. Translation of the second lens of the imaging system permits the imaging of selected cross-sections within the interaction region. The procedure for the laser and e-beam alignment looks as follows:

a) HeNe laser beam is introduced along the axis of the cell. Reflected by the flat Cu mirror the HeNe beam is visible to both, CCD and pyroelectric, cameras. Note that the HeNe laser beam should be in a flashing mode in order to be visible with a pyroviewer. This pulsing may be done with a chopper.

b) Adjust the translation axis of the second lens of the imaging system parallel to the HeNe beam direction to ensure that the HeNe spot image is stationary on both cameras when the different cross-section planes of the interaction region are imaged.

c) The HeNe laser spot, tightly focused within the interaction region and imaged by both cameras, may now be used as the position reference for the CO_2 laser beam as imaged with the pyroviewer and for e-beam flashing on phosphor screens and imaged by the CCD camera. Complete the alignment of the CO_2 and electron beam at the required resolution using pop-in phosphor screens to visualize the e-beam.

The described procedure shall ensure the alignment of the CO_2 and electron beam within the overlap region to the accuracy of ~ 10 μm.

Downstream of the interaction chamber, at the position of the electron spectrometer dipole, the electron beamline takes a 20° turn downward. For the LSLS experiment, the e-beam spectrum measurements are not very meaningful because just a slight, hardly resolved, broadening of the electron spectrum is expected due to the interaction with the laser beam. The dipole will serve to split the electrons from the copropagating x-rays that will be released through a foil membrane that caps a straight-ahead beamline behind the dipole. The x-ray spectrometer or any equipment intended to characterize or utilize the produced x-ray beam may occupy the space above and behind the electron spectrometer.

4 Conclusion

Not being intended as a formal proposal for the experiment, this paper is rather a feasibility study. Here, we have addressed the prospects of producing high-intensity picosecond, 1 Å x-ray beams via linear Compton backscattering using a 100-ps CO_2 laser and a high-brightness 70-MeV RF linac, both currently operational at the ATF.

A long-wavelength CO_2 laser and a high-γ electron beam seem to be an optimum combination when designing the LSLS for a particular x-ray region. To understand this, let us look again at the expressions for the wavelength (1), angular divergence (2), bandwidth (4), and power (16) of the backscattered radiation. As long as $\lambda_x=\lambda_L/4\gamma^2$ is considered as an invariant (the input design parameter), then choosing the CO_2 laser, with its wavelength 10 times longer than its rivals - solid state lasers, requires a $\sqrt{10}$ more energetic e-beam. This immediately improves the angular divergence of the produced x-rays which is equal to $1/\gamma$, and spectral bandwidth defined by $\Delta\gamma/\gamma$. According to $P_x \sim E_L\gamma^2$ (see (16)), the backscattered x-ray power will rise 10 times due to the higher γ. This stems from the facts that the x-ray flux is proportional to the delivered laser photon flux, and, at the fixed laser energy, the last parameter is proportional to λ_L.

When combining all mentioned above factors together, we come to the conclusion that using a CO_2 laser as the LSLS driver opens the prospective for up to 300 times increase in a spectral brightness of the produced x-rays to compare with a 1-μm laser of the same energy.

There is one drawback with the long-wavelength radiation that appears to compensate the aforementioned advantages - that is the λ_L-proportional diffraction divergence of the laser beam. Laser beam focusing to the 10 times bigger diffraction-limited spot may result in a 100 times drop of the x-ray power (if $r_b=r_L$) and in a 10,000 times drop in the brightness. However, it is not the true when we consider a practical scheme with the e-beam radius not less than ~10 μm. Then the CO_2 laser beam can be focused to this spot as well.

Note, also, that the backscattered x-ray pulse duration is defined primarily by the electron bunch length. Hence, the requirements to the short laser pulse duration are rather relaxed, at least for linear Compton scattering. The only limitation for the maximum pulse duration comes from a requirement of tight focusing of the laser beam over the Compton interaction range, that increases with the laser pulse length. The best way to solve this problem with a ~50-ps CO_2 laser is to channel it in a ~1-cm long waveguide of ~60-80 μm diameter. While requiring experimental verification, this approach looks promising for producing high-intensity x-ray fluxes. The high-brightness e-beam, available at the ATF, is the best fit to this scheme providing a possibility for filamentation of the relativistic electron bunches within a waveguide channel. Fluxes as high as 1.6×10^{22} photons/sec at a brightness of 2.5×10^{22} photons/sec.mm^{2}mrad^2 (@ 0.08% bandwidth) can be produced after the projected upgrade of the ATF CO_2 laser to the terawatt peak power level. The ATF x-ray source, which can exceed corresponding peak numbers obtained at the NSLS x-ray storage ring by several orders of magnitude, may be attractive for such applications as biological x-ray microscopy or the time-resolved fluorescence studies.

More than 10 Joules of the output energy in a several picosecond pulse will be demonstrated from the upgraded compact ATF CO_2 laser. Outputs above 100 J look feasible at further laser upscaling. The repetition rate of pulsed CO_2 lasers is limited by the gas exchange rate only. The state -of-the-art gas laser technology makes it feasible to build devices with a repetition rate of ≥100 Hz, an average power of ≥1 kW. This opens the prospects for constructing a high-power Laser Synchrotron X-Ray Sources desirable for various applications.

Let us finally address the prospects of the nonlinear Compton scattering studies using a terawatt-class CO_2 laser. With a 3-TW CO_2 laser beam focused into a 30 μm diameter spot, as high as 10^{17} W/cm^2 intensity will be attained. According to the expression

$$a = 0.85 \times 10^{-9} \lambda[\mu m] I^{1/2}[W/cm^2],$$

such intensity corresponds to the unitless laser strength of a=3. It is known that at a>1, the nonlinear Compton scattering effect comes to scene. With the maximum order of generated harmonics being equal to $n=a^3$, as short as λ=0.03 Å radiation may be produced when a CO_2 laser beam is backscattered by the 70-MeV e-beam. After the further feasible upgrade of the ATF linac to 140 MeV, even shorter ~0.01 Å x-rays may be produced via nonlinear Compton backscattering. In Fig.11, the intensity of harmonics is plotted as a function of a. For a=3 and $(a^2/4)(1+a^2/2) = 0.41$, the maximum of the intensity distribution shifts to n=11-13 with these components ~3 times more intense than the fundamental n=1 component.

Other interesting features of harmonics are that their angular divergence and spectral bandwidth are inversely proportional to n offering prospects for considerable increase in spectral brightness. Thus, with a terawatt CO_2 laser, the expected nonlinear Compton scattering effect is not just of a basic scientific interest but may be used for a significant expansion of the x-ray spectrum to benefit the potential applications. Study of nonlinear Compton scattering may be carried out as the next stage of the ATF LSLS experiment. Such study has been a subject of the former proposal [7] and is not discussed here in further details.

References

1. NSLS Annual Report 1992, BNL 52371 (1993).
2. R. Kluffky, private communication.
3. H.C. Kapteyn, L.B. Da Silva, and R.W. Falcone,"Short-Wavelength Lasers", Proc. IEEE, **80**, 342 (1992).
4. C. Pelligrini, et. al., "A 2-4 nm High Power FEL on the SLAC Linac", Nucl. Instrum. and Methods in Phys. Res., A **331**, 223 (1993).
5. E. Esarey, P. Sprangle, and S.K. Ride, "Nonlinear Thomson Scattering of Intense Laser Pulses from Beams and Plasmas", Preprint NRL/MR/6790-93-7365 (1993).
6. J. Kirz, C. Jacobsen, and M. Howells, "Soft X-ray Microscopes and Their Biological Applications", Preprint LBL-36371/UC-410 (1994).
7. R.C. Fernow, H.G. Kirk, J. Rogers, I.J. Bigio, N.A. Kurnit, T. Shimada, K.T. McDonald, D.P. Russel, and M.E. Wall, "Proposal for an Experimental Study of Nonlinear Compton Scattering", Preprint DOE/ER/3072-55 (1989).
8. R.C. Fernow, "Magnetic Design for the ATF Beamline #1 ", Preprint BNL-47117 (1992).
9. R. Fernow, "New Final Focus Design for the ICA Experiment", Draft (1995).
10. I.V. Pogorelsky, ATF CO_2 Laser System Upgrade to Terawatt Peak Power", Preprint BNL-61859 (1995).
11. I.V. Pogorelsky, "Electron Acceleration in Plasma Channels with Terawatt CO_2 Lasers", Preprint BNL-61482 (1995).
12. I.V. Pogorelsky, J. Fischer, K.P. Kusche, M. Babzien, N.A. Kurnit, I.J. Bijio, R.F. Harrison, and T. Shimada, "Subnanosecond Multi-Gigawatt CO_2 Laser", IEEE J. of Quant. Electron., **31**, 556 (1995).

TABLES

Table 1 Operational Characteristics of NSLS x-ray beamline

X-ray Storage Ring Parameters	
Electron Energy	2.58 GeV
Average Current	0.25 A
Circumference	170 m
Electron Orbital Period	568 ns
RF Frequency	52.88 MHz
Bunch Length (2σ)	10.5 cm
Number of RF Buckets	30
Energy Spread	0.08%
Horizontal Emittance	0.1 mm.mrad
Vertical Emittance	0.001 mm.mrad
Optical Characteristics @5 keV in Regular Mode (30 bunches per revolution)	
Repetition Rate	52.88 MHz
Photons per Pulse	4×10^{7}
Average Flux (/0.1%b.w./5 mrad)	2×10^{15} photons/sec
Peak Flux (/0.1%b.w./5 mrad)	1.2×10^{17} photons/sec
Average Brightness (/0.1%b.w.)	10^{18}photons/sec.mm^{2}mrad^2
Peak Brightness (/0.1%b.w.)	5×10^{19}phot/sec.mm^{2}mrad^2
Optical Characteristics @5 keV in Timing Mode (1 bunch per revolution)	
Repetition Rate	1.76 MHz
Photons per Pulse	10^{9}
Peak Flux (/0.1%b.w./5 mrad)	3×10^{18} photons/sec
Peak Brightness (/0.1%b.w.)	$7.5\times$ 10^{20}phot/sec.mm^{2}mrad^2

Table 2 ATF Lasers and e-Beam Performance

LINAC	
Electron Energy [MeV]	50-70
Peak Current [A]	50
Bunch Duration FWHM [ps]	10
Repetition Rate [Hz]	3
Normalized Emittance [mm.mrad]	2
Electron Momentum Spread [relative]	0.2%
YAG Laser	
Total IR Energy	30 mJ
IR Energy Split to CO_2 Laser	20 mJ
UV energy	0.3 mJ
UV Pulse Duration FWHM	12 ps
Spot Size on Cathode [$1/e^2$ Ø]	0.1-1 mm
Pulse Timing Jitter	<1 ps
Pulse Duration Jitter	<1 ps
Energy Jitter	3%
CO_2 Laser (Present)	
Oscillator Peak Power [MW]	1
Oscillator Pulse Duration [ns]	100
Switched Pulse Duration [ps]	~300
Double Sliced Pulse Duration [ps]	10-300
Amplified Pulse Duration [ps]	100
Output Energy [J]	1
Output Peak Power [GW]	10
Repetition Rate [Hz]	0.1
CO_2 Laser (Upgrade)	
Amplified Pulse Duration [ps]	3-50
Output Energy [J]	3-30
Output Peak Power [TW]	~1
Repetition Rate [Hz]	0.1

Table 3 ATF LSLS (1st Stage) Design Parameters

ELECTRON BEAM	
Energy [MeV]	70
Bunch Charge [nC]	0.5
Bunch Duration FWHM [ps]	10(3)
Radius at Focus [μm]	140
Waist Length [mm]	>>10
Normalized Emittance [mm.mrad]	2
Electron Momentum Spread [relative]	0.2(0.05)%
CO_2 LASER	
Pulse Duration [ps]	100
Peak Power [GW]	10
Radius at Focus [μm]	140
Waist Length [mm]	17
X RAYS	
Wavelength [Å]	1.325 /9.36 keV/
Pulse Duration [ps]	**10(3)**
Angular Spread [mrad]	7
Spectral Bandwidth [relative]	0.4(0.12)%
Photons per Pulse	1.7×10^{8}
Peak Flux [photons/s]	**$1.7(5.3)\times10^{19}$**
Peak Brightness [phot/sec.mm^{2}mrad^2]	(10^{18})

* Framed and boldfaced are the parameters where the LSLS outperforms the standard SLS (compare with the NSLS x-ray ring parameters in Table 1).

Table 4 ATF LSLS (2nd Stage) Design Parameters

(@ 0.3-TW, 50-ps CO_2 laser pulse)

ELECTRON BEAM	
Energy [MeV]	70(140)
Bunch Charge [nC]	0.5
Bunch Duration FWHM [ps]	3
Radius at Focus [μm]	140
Waist Length [mm]	>>10
Normalized Emittance [mm.mrad]	2(1)
Electron Momentum Spread [relative]	0.05(0.025)%
CO_2 LASER	
Pulse Duration [ps]	50
Peak Power [TW]	0.3
Radius at Focus [μm]	100
Waist Length [mm]	9
X RAYS	
Wavelength [Å]	1.325(0.33)
Pulse Duration [ps]	**3**
Angular Spread [mrad]	7(3.5)
Spectral Bandwidth [relative]	0.12(0.08)%
Photons per Pulse	**2.5×10^{9}**
Peak Flux [photons/sec]	**8×10^{20}**
Peak Brightness [phot/sec.mm^{2}mrad^2]	$1.5\times10^{19}(6\times10^{19})$

* Framed and boldfaced are the parameters where the LSLS outperforms the standard SLS (compare with the NSLS x-ray ring parameters in Table 1).

Table 5 ATF LSLS (2nd Stage) Design Parameters

(@ 1-TW, 5-ps CO_2 laser pulse)

ELECTRON BEAM	
Energy [MeV]	70(140)
Bunch Charge [nC]	0.5
Bunch Duration FWHM [ps]	3
Radius at Focus [μm]	40
Waist Length [mm]	>10
Normalized Emittance [mm.mrad]	2(1)
Electron Momentum Spread [relative]	0.05(0.025)%
CO_2 LASER	
Pulse Duration [ps]	5
Peak Power [TW]	1
Radius at Focus [μm]	30
Waist Length [mm]	1.2
X RAYS	
Wavelength [Å]	1.325(0.33)
Pulse Duration [ps]	**3**
Angular Spread [mrad]	7(3.5)
Spectral Bandwidth [relative]	0.6%
Photons per Pulse	**1.5×10^{10}**
Peak Flux [photons/sec]	**5×10^{21}**
Peak Brightness [phot/sec.mm^{2}mrad^2]	**$2\times10^{21}(8\times10^{21})$**

* Framed and boldfaced are the parameters where the LSLS outperforms the standard SLS (compare with the NSLS x-ray ring parameters in Table 1).

Table 6 ATF LSLS (2nd Stage) Design Parameters

(@ **channeled** 0.3-TW, 50-ps CO_2 laser pulse)

ELECTRON BEAM	
Energy [MeV]	70(140)
Bunch Charge [nC]	0.5
Bunch Duration FWHM [ps]	3
Radius at Focus [μm]	40
Waist Length [mm]	>>10
Normalized Emittance [mm.mrad]	2(1)
Electron Momentum Spread [relative]	0.05(0.025)%
CO_2 LASER	
Pulse Duration [ps]	50
Peak Power [TW]	0.3
Radius at Focus [μm]	30
Channel Length [mm]	10
X RAYS	
Wavelength [Å]	1.325(0.33)
Pulse Duration [ps]	**3**
Angular Spread [mrad]	7(3.5)
Spectral Bandwidth [relative]	0.12(0.08)%
Photons per Pulse	**5×10^{10}**
Peak Flux [photons/sec]	**1.6×10^{22}**
Peak Brightness [phot/sec.mm^{2}mrad^2]	**$6\times10^{21}(2.5\times10^{22})$**

* Framed and boldfaced are the parameters where the LSLS outperforms the standard SLS (compare with the NSLS x-ray ring parameters in Table 1).

Drawings Captions

Fig.1. Wavelength compression via relativistic Compton scattering:
a) in the laboratory frame, electron interacts with a counter-propagating EM wave of frequency ν_L;
b) in the relativistic frame, electron interacts with the wave of frequency $2\nu_L$ and radiates secondary EM waves in forward and backward directions at the same frequency of $2\nu_L$;
c) in the laboratory frame, backscattered radiation has a frequency of $\nu_x=4\gamma^2\nu_L$.

Fig.2. No backscattered photons should appear beyond the cone with the apex angle of $\theta=1/\gamma$.

Fig.3. X-ray pulse length is defined primarily by the electron bunch duration. The relative position of pulses at the beginning and to the end of the interaction is shown for two conditions: a) $\tau_L < \tau_b$ and b) $\tau_L > \tau_b$. For any condition, $\tau_x \approx \tau_b$, because the component dependent upon τ_L is usually negligibly small, for the relativistic electrons.

Fig.4. Diagram of the ATF .

Fig.5. Schematic of the beamline #1.

Fig.6. ATF laser system consists of CO_2 and Nd:YAG lasers. The joint application of lasers is illustrated by the example of the projected Compton Scattering experiment.

Fig.7. Equivalent scheme of focusing optics

Fig.8 Possible configuration of reflective focusing elements.

Fig.9. Axicon telescope.

Fig.10 Configuration of the LSLS experiment

Fig. 11. The intensity of harmonics in a nonlinear Compton scattering as a function of a unitless laser strength a. [5]

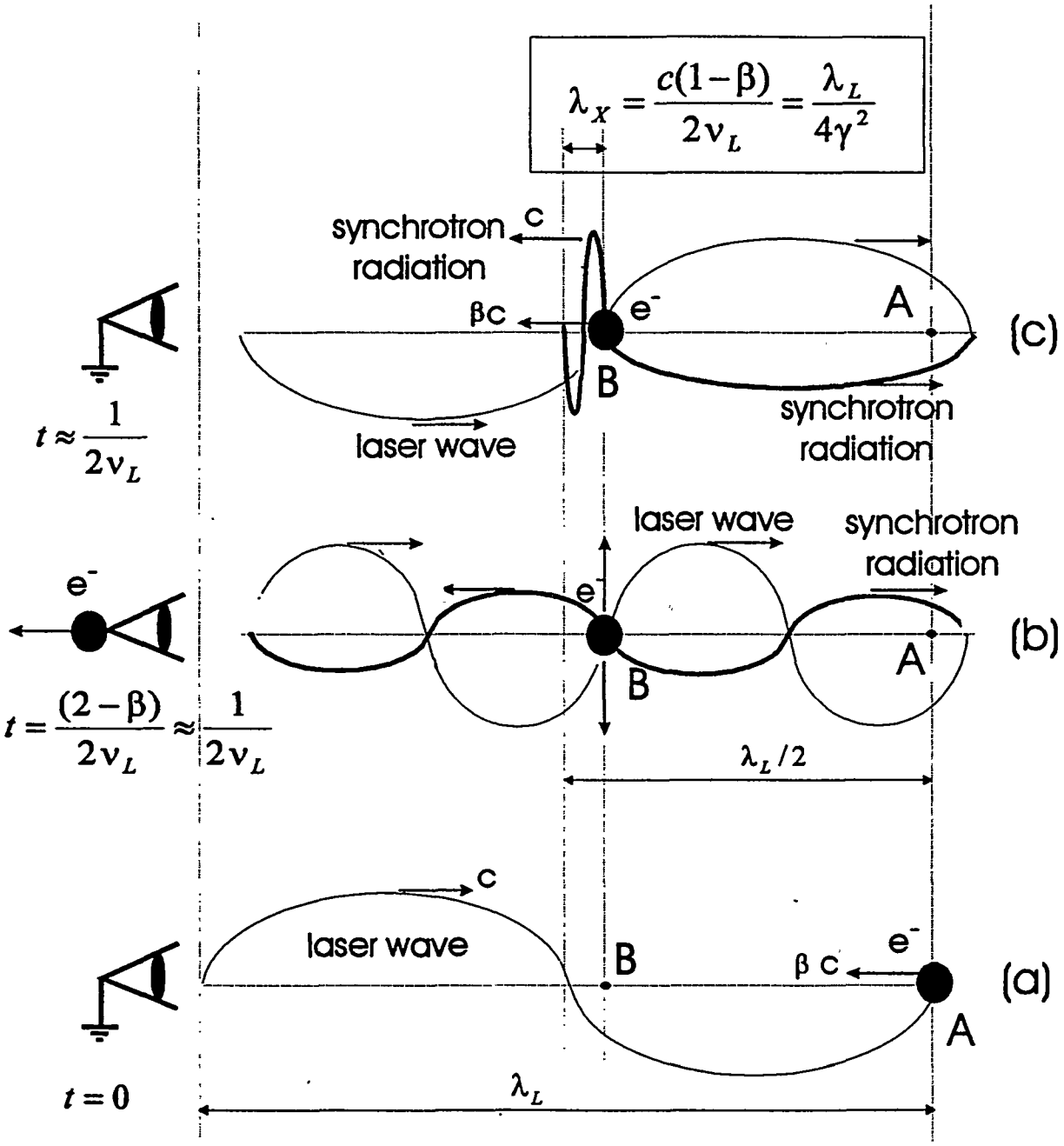
$\lambda_X = \frac{c(1-\beta)}{2\nu_L} = \frac{\lambda_L}{4\gamma^2}$
synchrotron radiation
c
βc
e⁻
A
B
(c)
synchrotron radiation
laser wave
$t \approx \frac{1}{2\nu_L}$
laser wave
synchrotron radiation
e⁻
e⁻
A
B
(b)
$t = \frac{(2-\beta)}{2\nu_L} \approx \frac{1}{2\nu_L}$
$\lambda_L/2$
c
laser wave
B
β c
e⁻
(a)
A
$t = 0$
λ_L

Fig. 1

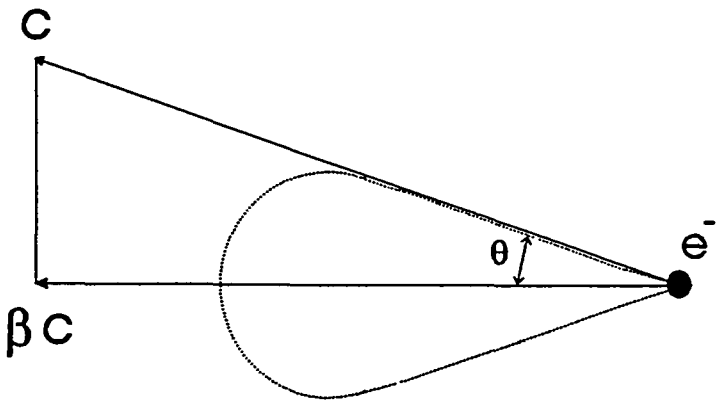

$$c\cos\theta = c\beta$$

$$\downarrow \qquad \downarrow$$

$$1-\theta^2/2 = 1-1/2\gamma^2$$

$$\downarrow$$

$$\theta = 1/\gamma$$

Fig.2

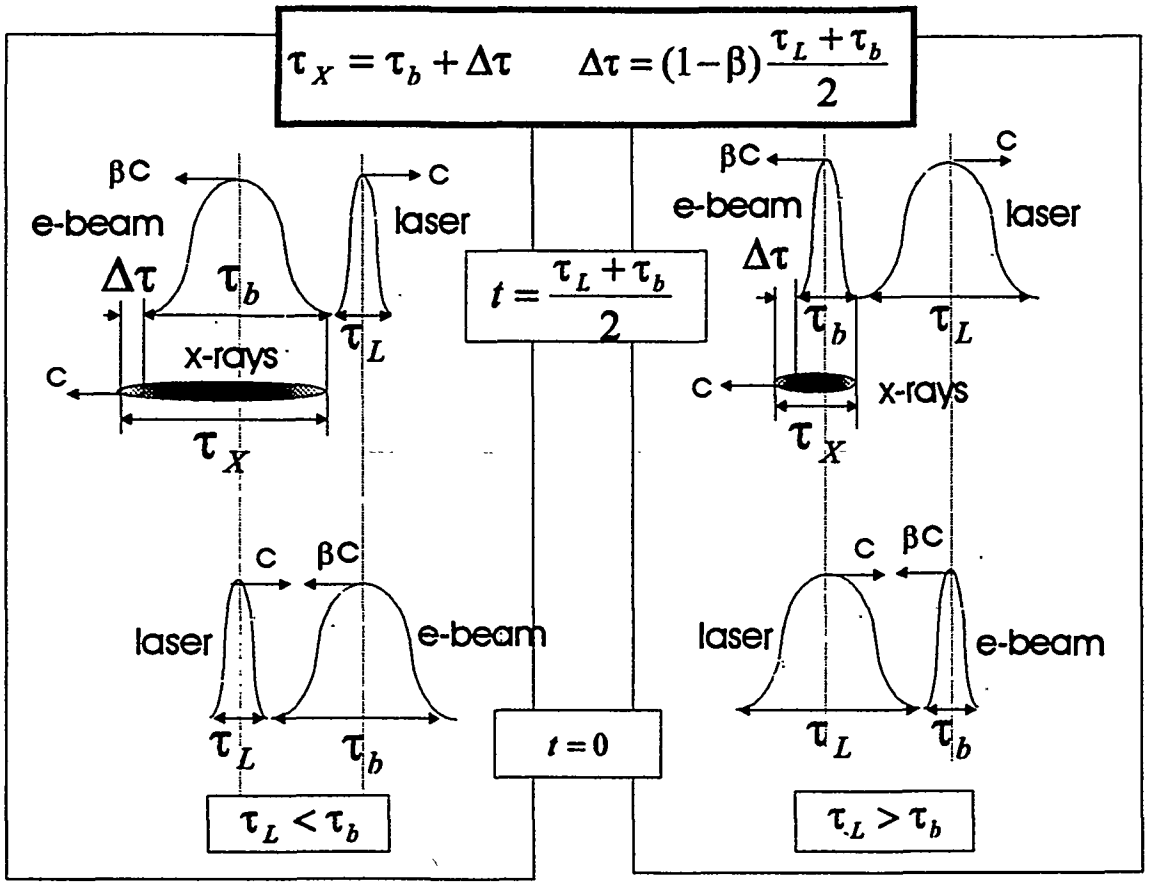
$\tau_X = \tau_b + \Delta\tau \qquad \Delta\tau = (1-\beta)\frac{\tau_L + \tau_b}{2}$
βc
e-beam
c
laser
Δτ
τ_b
τ_L
x-rays
c
τ_X
$t = \frac{\tau_L + \tau_b}{2}$
βc
c
e-beam
laser
Δτ
τ_b
τ_L
c
x-rays
τ_X
c
βc
laser
e-beam
τ_L
τ_b
$t = 0$
$\tau_L < \tau_b$
c
βc
laser
e-beam
τ_L
τ_b
$\tau_L > \tau_b$

Fig. 3

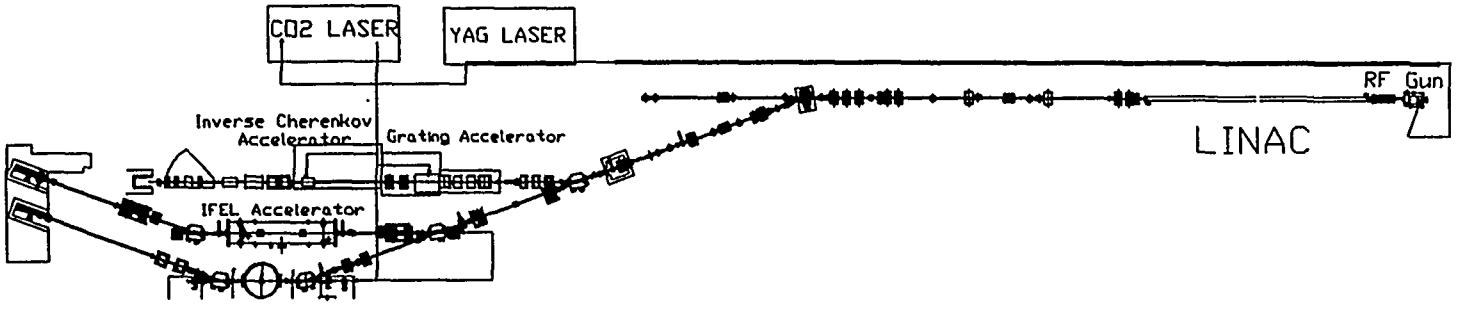
CO2 LASER
YAG LASER
RF Gun
Inverse Cherenkov Accelerator
Grating Accelerator
LINAC
IFEL Accelerator

Fig.4

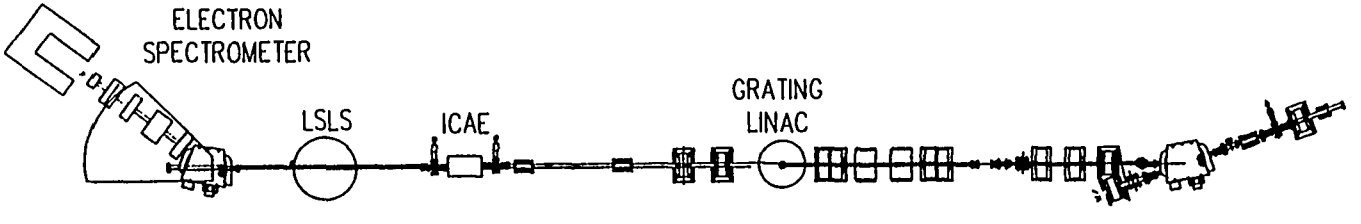
ELECTRON SPECTROMETER
LSLS
ICAE
GRATING LINAC

Fig.5

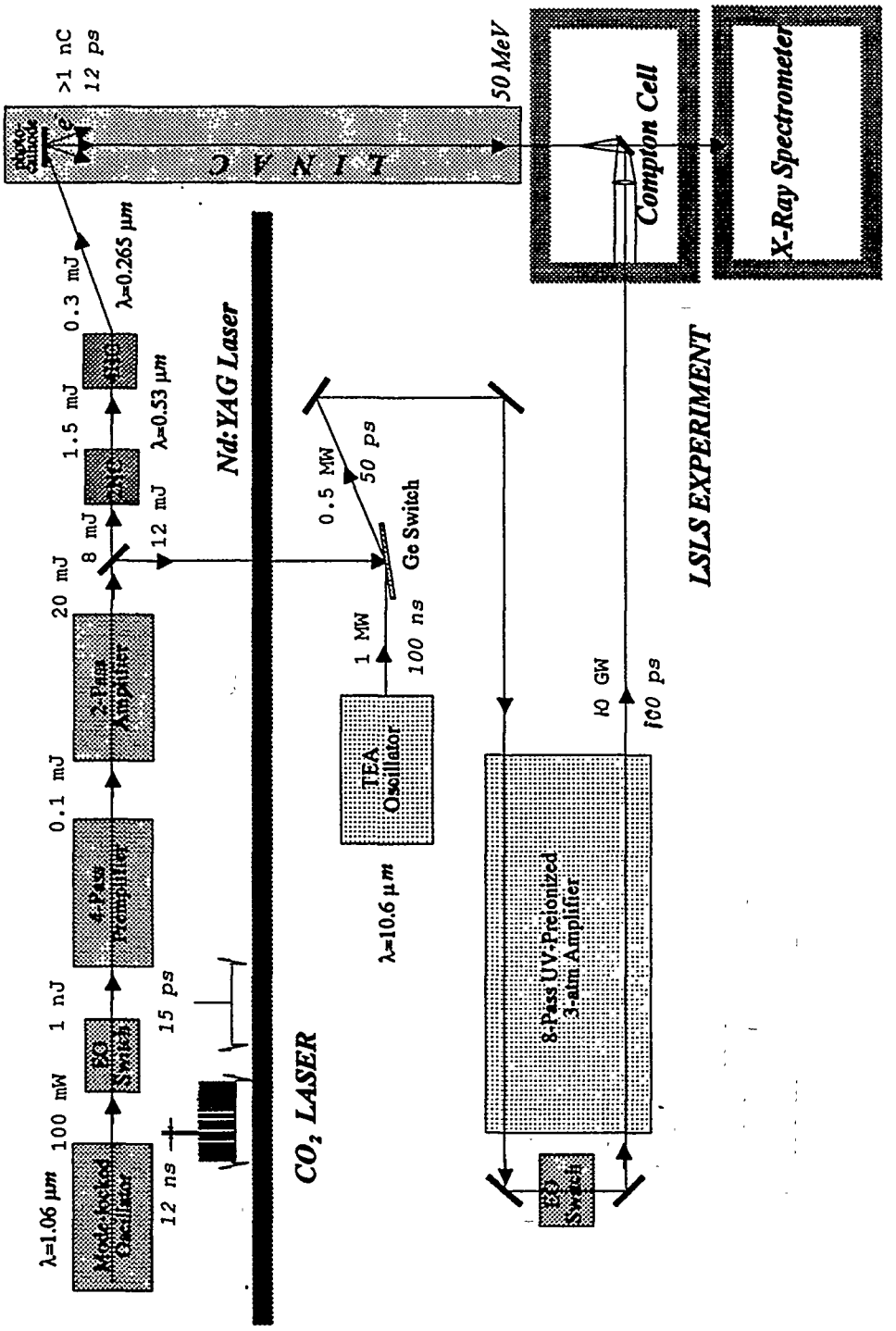
>1 nC
12 ps
50 MeV
Compton Cell
X-Ray Spectrometer
LSLS EXPERIMENT
Nd:YAG Laser
CO2 LASER
λ=1.06 μm
100 mW
1 nJ
15 ps
12 ns
EO Switch
4-Pass Preamplifier
0.1 mJ
2-Pass Amplifier
20 mJ
8 mJ
12 mJ
1.5 mJ
0.3 mJ
λ=0.53 μm
λ=0.265 μm
0.5 MW
50 ps
Ge Switch
1 MW
100 ns
TEA Oscillator
λ=10.6 μm
10 GW
100 ps
8-Pass UV-Preionized 3-atm Amplifier
EO Switch

Fig.6

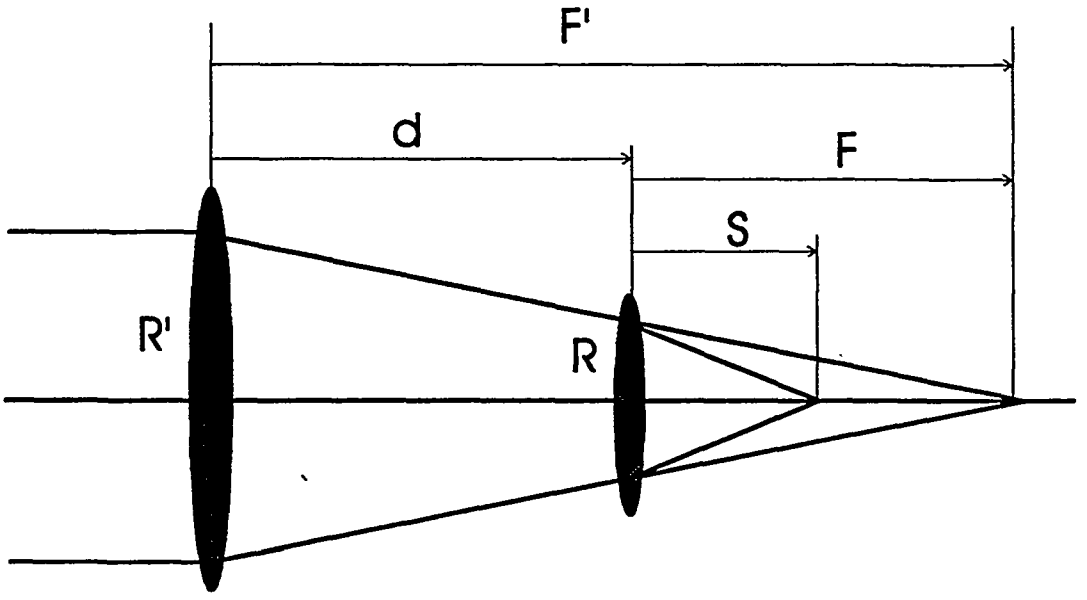

Fig.7

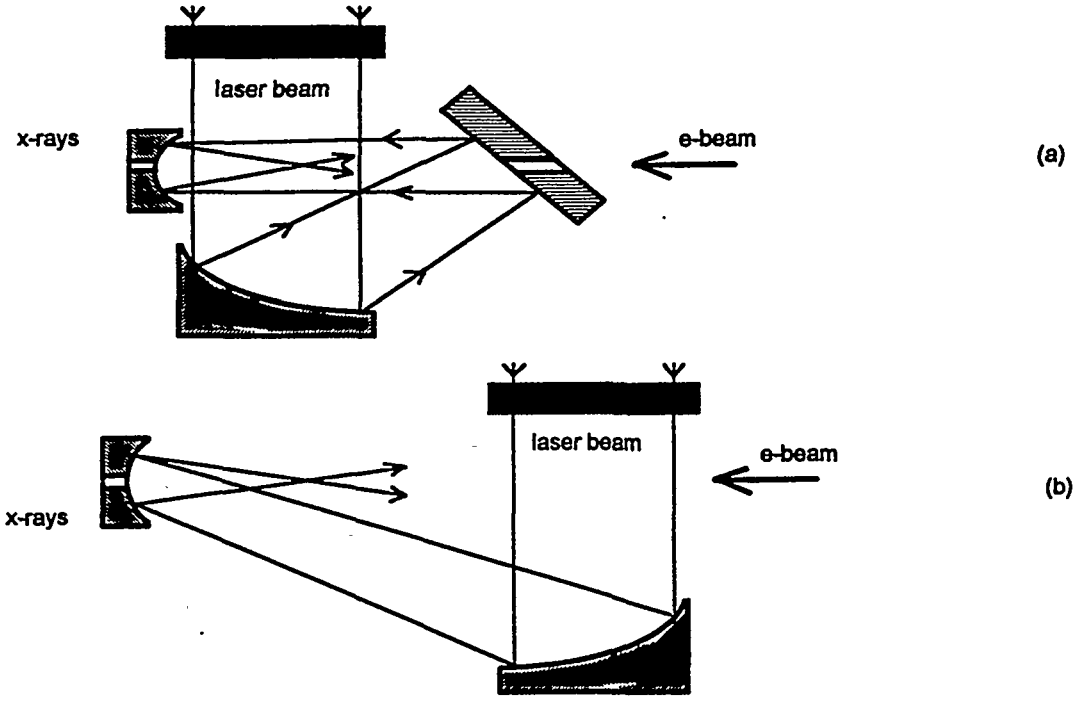

Fig.8

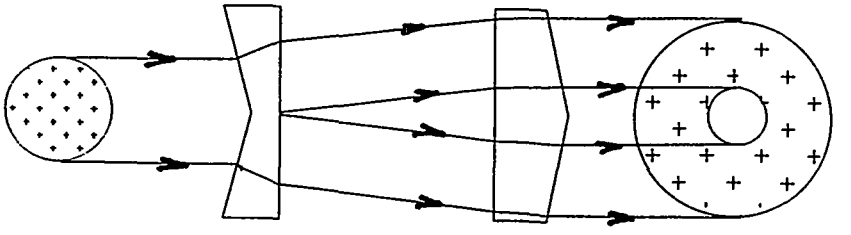

Fig.9

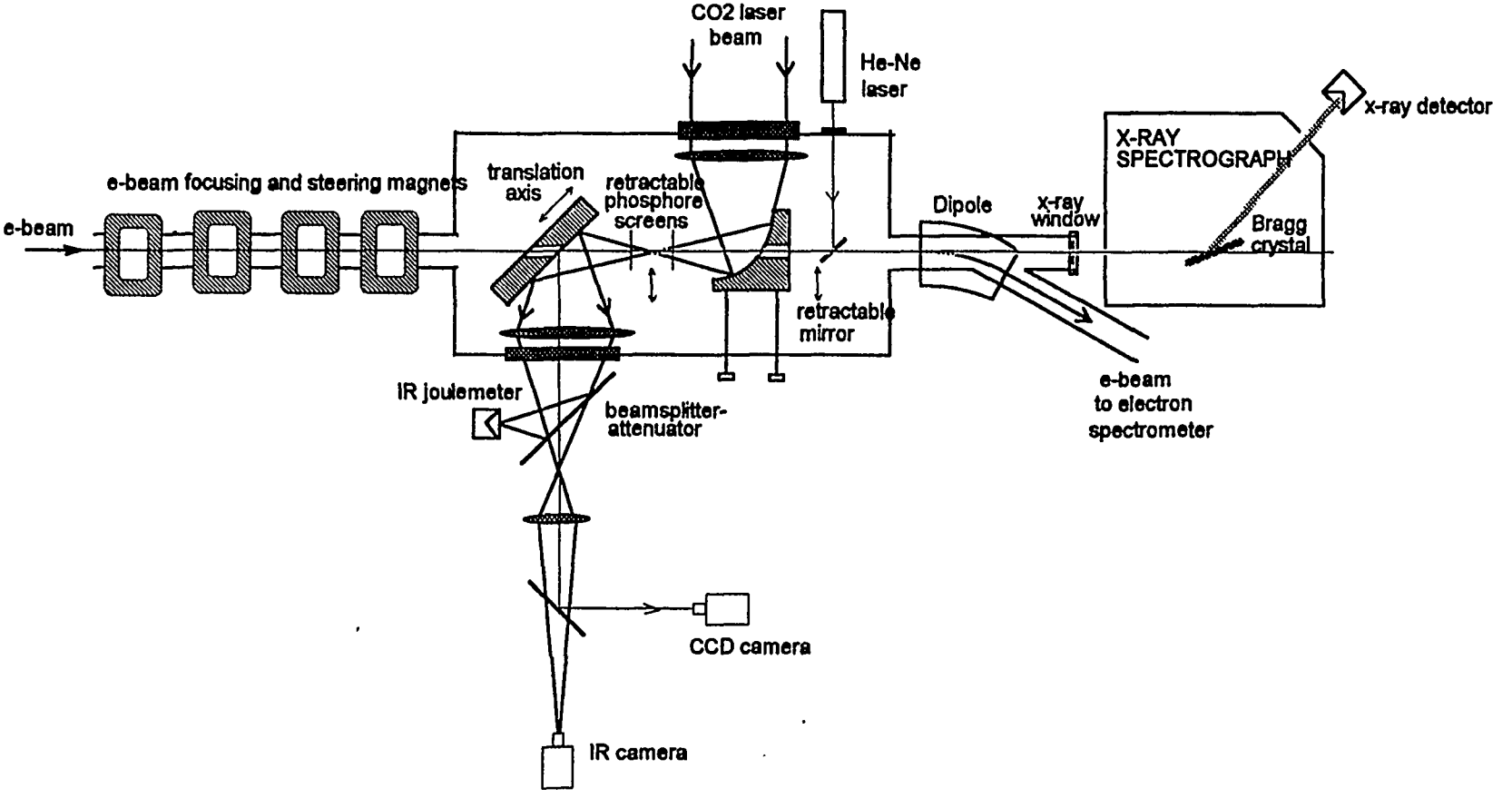
CO2 laser beam
He-Ne laser
x-ray detector
X-RAY SPECTROGRAPH
e-beam focusing and steering magnets
translation axis
retractable phosphore screens
Dipole
x-ray window
Bragg crystal
e-beam
retractable mirror
IR joulemeter
beamsplitter-attenuator
e-beam to electron spectrometer
CCD camera
IR camera

Fig.10

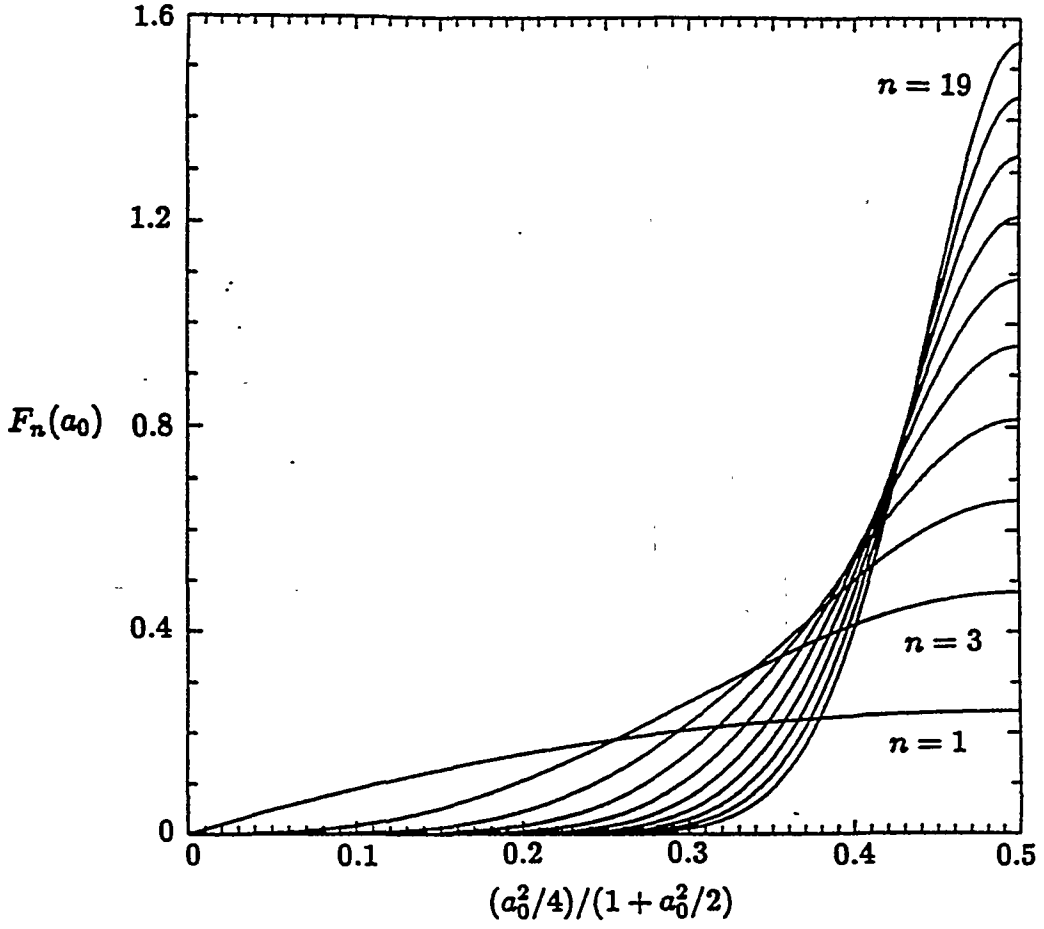

Fig.11